Charmless B decay reconstruction in 2019 data

(The Belle II Collaboration)

Abstract

We report on the reconstruction of various charmless B decays from electron-positron collisions at the energy corresponding to the $\Upsilon(4S)$ resonance collected with the Belle II detector at the SuperKEKB collider. We use simulation to devise optimized event selections and apply them to the full data set collected in 2019, corresponding to $8.7\,\mathrm{fb}^{-1}$ of integrated luminosity. We fit the difference between half of the collision energy and the B candidate energy (in the $\Upsilon(4S)$ frame) for events restricted to a signal-rich range in beam-energy-constrained mass to search for charmless signals. Signal yields of approximately 80, 15, 20, 30, 90, and 160 decays are reconstructed for the channels $B^0 \to K^+\pi^-$, $B^0 \to \pi^+\pi^-$, $B^+ \to K^0_S(\to \pi^+\pi^-)\pi^+$, $B^+ \to K^+\pi^0(\to \gamma\gamma)$, $B^+ \to K^+K^-K^+$, and $B^+ \to K^+\pi^-\pi^+$, respectively. Yields and background contaminations are compatible with those expected from simulation and comparable with those obtained by the Belle experiment. The results show a good understanding of the detector performance and offer a reliable basis to assess projections for future reach.

1. INTRODUCTION AND MOTIVATION

The study of charmless B decays is a keystone of the Belle II physics program, which offers the unique capability of studying jointly, within a consistent experimental environment, all relevant two-, three-, and multi-body final states. This ability can enable significant advances, including an improved determination of the quark-mixing-matrix angle ϕ_2/α, a conclusive understanding of long-standing anomalies like the so-called $K\pi$ puzzle, and a thorough investigation of charge-parity-violating asymmetries localized in the phase space of three-body B decays. Ultimately, the Belle II charmless program is expected to offer a sharper picture of the weak interactions of quarks that could reveal possible deviations from the standard model [1].

The Belle II detector, complete with its vertex detector, started its 2019 collision operations on March 11 and continued until December 13. The collected sample of electron-positron collisions corresponds to an integrated luminosity of $8.7\,\text{fb}^{-1}$ at the $\Upsilon(4S)$ resonance and $0.827\,\text{fb}^{-1}$ at an energy about $60\,\text{MeV}$ smaller. This document describes the reconstruction of charmless signals in addition to the 25 $B^0 \to K^+\pi^-$ decays reconstructed in Fall 2019 using half of the current data set [2].

We focus on two- and three-body charmless decays with branching fractions of 10^{-6}, or larger, into final states sufficiently simple to obtain visible signals in the current data set with a relatively straightforward reconstruction. The target decay modes are $B^0 \to K^+\pi^-$, $B^0 \to \pi^+\pi^-$, $B^+ \to K_S^0(\to \pi^+\pi^-)\pi^+$, $B^+ \to K^+\pi^0(\to \gamma\gamma)$, $B^+ \to K^+K^-K^+$, and $B^+ \to K^+\pi^-\pi^+$. Charge-conjugate processes are implied in what follows.

The reconstruction strategy and procedures are developed and finalized in simulated data prior to applying it to the experimental data. Experimental and simulated data are then compared in terms of signal yields, backgrounds, and relevant resolutions. Most of the analysis is conducted using two variables known to be strongly discriminating between B signal and background from $e^+e^- \to q\bar{q}$ continuum events, where q indicates any quark of the first or second family,

- the energy difference $\Delta E \equiv \sqrt{s}/2 - E_B^*$ between half of the collision energy and the total energy of the reconstructed B candidate, both in the $\Upsilon(4S)$ frame;

- the beam-energy-constrained mass $M_{\text{bc}} \equiv \sqrt{s/4 - (p_B^*)^2}$, which is the invariant mass of the B candidate where the B energy is replaced by the (more precisely known) half of the collision energy.

2. THE BELLE II DETECTOR

Belle II is a particle-physics detector [1, 3], designed to reconstruct the products of electron-positron collisions produced by the SuperKEKB asymmetric-energy collider [4], located at the KEK laboratory in Tsukuba, Japan. Belle II comprises several subdetectors arranged around the interaction space-point in a cylindrical geometry. The innermost subdetector is the vertex detector, which uses position-sensitive silicon layers to sample the trajectories of charged particles (tracks) in the vicinity of the interaction region to extrapolate the decay positions of their long-lived parent particles. The vertex detector includes two inner layers of silicon pixel sensors and four outer layers of silicon microstrip sensors. The

second pixel layer is currently incomplete and covers only a small portion of azimuthal angle. Charged-particle momenta and charges are measured by a large-radius, helium-ethane, small-cell central drift chamber, which also offers charged-particle-identification information through a measurement of particles' energy-loss by specific ionization. A Cherenkov-light angle and time-of-propagation detector sourrounding the chamber provides charged-particle identification in the central detector volume, supplemented by proximity-focusing, aerogel, ring-imaging Cherenkov detectors in the forward regions. A CsI(Tl)-crystal electromagnetic calorimeter allows for energy measurements of electrons and photons. A solenoid surrounding the calorimeter generates a uniform axial $1.5\,\mathrm{T}$ magnetic field filling its inner volume. Layers of plastic scintillator and resistive-plate chambers, interspersed between the magnetic flux-return iron plates, allow for identification of K_{L}^0 and muons. The subdetectors most relevant for this work are the silicon vertex detector, the tracking drift chamber, the particle-identification detectors, and the electromagnetic calorimeter.

3. SELECTION AND RECONSTRUCTION

We reconstruct the following two-body decays:

- $B^0 \to K^+ \pi^-$,

- $B^0 \to \pi^+ \pi^-$,

- $B^+ \to K_{\mathrm{S}}^0 (\to \pi^+ \pi^-) \pi^+$,

- $B^+ \to K^+ \pi^0 (\to \gamma\gamma)$,

and three-body decays:

- $B^+ \to K^+ K^- K^+$,

- $B^+ \to K^+ \pi^+ \pi^-$.

In addition, we use the control channel $B^+ \to \overline{D}^0 (\to K^+ \pi^- \pi^0) \pi^+$ for validation of continuum-suppression discriminating variables and optimization of the π^0 selection.

3.1. Data

We use generic simulated data to optimize the event selection and compare the final ΔE distributions observed in experimental data with expectations. We use signal-only simulated data to model relevant signal features for fits. Generic simulation consists of Monte Carlo samples that include $B^0\overline{B}^0$, B^+B^-, $u\bar{u}$, $d\bar{d}$, $c\bar{c}$, and $s\bar{s}$ processes in realistic proportions and correspond to an integrated luminosity of $50\,\mathrm{fb}^{-1}$, about six times the $\Upsilon(4S)$ data. In addition, 2×10^6 signal-only events are generated for each channel. Three-body decays are generated assuming phase-space distributions.

As for experimental data, we use all 2019 $\Upsilon(4S)$ good-quality runs, corresponding to an integrated luminosity of $8.7\,\mathrm{fb}^{-1}$. All events are required to meet mild data-skim selection criteria, based on total energy and charged-particle multiplicity in the event, targeted at reducing sample sizes to a manageable level.

3.2. Reconstruction and baseline selection

We form final-state particle candidates by applying loose baseline selection criteria and then combine them in kinematic fits consistent with the topologies of the desired decays to reconstruct intermediate states and B candidates.

We reconstruct charged pion and kaon candidates by starting from the most inclusive charged-particle classes and by requiring fiducial criteria that restrict them to the full acceptance in the central drift chamber and to loose ranges in impact parameter to reduce beam-background-induced tracks, which do not originate from the interaction region preferably. We reconstruct neutral pion candidates by requiring photons to exceed energies of about 20 MeV, restricting the diphoton mass, and excluding extreme helicity-angle values to suppress combinatorial background from collinear soft photons. The mass of the π^0 candidates is constrained to its known value in subsequent kinematic fits. For K^0_S reconstruction, we use pairs of opposite-charge red particles that originate from a common space-point and have dipion mass consistent with a K^0_S. The resulting $K^\pm$, $\pi^\pm$, π^0, and K^0_S candidates are combined through kinematic fits into each of our target signal channels, consistent with the desired topology. Because we use flavor-tagging information as input to the continuum-background discriminator, we reconstruct the vertex of the accompanying tag-side B mesons using all tracks in the tag-side and identify the flavor using a category-based flavor tagger [5]. The reconstruction of the control channel is conceptually similar, except for the requirement $1.84 < m(K^-\pi^+\pi^0) < 1.89\,\mathrm{GeV}/c^2$ on the $K^-\pi^+\pi^0$ mass to be consistent with the known D^0 meson mass.

Simulation is used to identify and suppress contamination from peaking backgrounds, that is, misreconstructed events clustering in the signal region $M_{\mathrm{bc}} > 5.27\,\mathrm{GeV}/c^2$ and $-0.15 < \Delta E < 0.15$ GeV. Relevant peaking backgrounds affect only the $B^+ \to K^+\pi^-\pi^+$ channel. Background from $B^+ \to \overline{D}^0(\to K^+\pi^-)\pi^+$ decays is suppressed by vetoing candidates with kaon-pion mass $1.84 < m(K^+\pi^-) < 1.89\,\mathrm{GeV}/c^2$. The contribution from $B^+ \to J/\psi(\to \mu^+\mu^-)K^+$ decays where muons are misidentified as pions is suppressed by vetoing candidates with dipion mass $3.05 < m(\pi^+\pi^-) < 3.15\,\mathrm{GeV}/c^2$.

3.3. Continuum suppression

The main challenge in reconstructing significant charmless signals is the large contamination from continuum background. To discriminate against such background, we use a binary boosted decision-tree classifier that combines nonlinearly a number of variables known to provide statistical discrimination between B-meson signals and continuum. We choose 39 variables whose correlation with ΔE and M_{bc} is below $\pm 5\%$ to avoid biases in signal-yield determination. These variables include quantities associated to event topology (global and signal-only angular configurations), flavor-tagger information, vertex separation and uncertainty information, and kinematic-fit quality information. Data-simulation comparison for input distributions using the control sample shows no major inconsistency for both signal and background. We train the classifier to identify statistically signal and background features using unbiased simulated samples.

4

4. OPTIMIZATION OF THE SIGNAL SELECTION

For each channel, we optimize the selection to isolate abundant, low-background signals using simulated and control-sample data. We vary the selection criteria on continuum-suppression output, charged-particle identification information, and choice of π^0 (when appropriate) to maximize $S/\sqrt{S + B}$, where S and B are signal and background yields, respectively, estimated in the ΔE signal region. Continuum-suppression and particle-identification requirements are optimized simultaneously using simulated data. The π^0 selection is optimized independently by using control $B^+ \to \overline{D}^0(\to K^+\pi^-\pi^0)\pi^-$ decays in which S is the $B^+ \to \overline{D}^0(\to K^+\pi^-\pi^0)\pi^-$ signal yield, scaled to the expected $B^+ \to K^+\pi^0$ yield, and B is the background observed in an M_{bc} sideband of $B^+ \to K^+\pi^0$.

5. DETERMINATION OF SIGNAL YIELDS

More than one candidate per event populates the resulting ΔE distributions, with average multiplicities ranging from 1.00 to 1.25. We restrict to one candidate per event as follows. For channels with π^0, we first select the π^0 candidate with the highest p-value of the mass-constrained diphoton fit. If more than one candidate remains, and for all other channels, we select a single B candidate randomly.

Signal yields are determined with maximum likelihood fits of the unbinned ΔE distributions of candidates restricted to the signal region in M_{bc}. Fit models are generally determined empirically by using simulation, with the only additional flexibility of a global shift of peak positions when suggested by likelihood-ratio tests.

6. RESULTS

Figures 1–6 show the resulting ΔE distributions, with fit results overlaid. Prominent narrow signals of 10–150 events are visible overlapping smooth backgrounds dominated by continuum. The $B^0 \to K^+\pi^0$ signal shows a low-ΔE tail, due to resolution effects in π^0 reconstruction. Satellite signals from kinematically similar misreconstructed decays are visible in the $B^0 \to K^+\pi^-$, $B^0 \to \pi^+\pi^-$, and $B^+ \to K^+\pi^-\pi^-$ decays.

Decay	Yield		Yield/fb^{-1}	
	MC	Data	MC	Data
$B^0 \to K^+\pi^-$	371 ± 24	79 ± 11	7.4 ± 0.5	9.1 ± 1.3
$B^0 \to \pi^+\pi^-$	78 ± 11	16 ± 5	1.6 ± 0.2	1.8 ± 0.6
$B^+ \to K_S^0\pi^+$	83 ± 10	18 ± 5	1.7 ± 0.2	2.1 ± 0.6
$B^+ \to K^+\pi^0$	191 ± 20	27 ± 8	3.8 ± 0.4	3.1 ± 0.9
$B^+ \to K^+K^+K^-$	559 ± 28	92 ± 12	11.2 ± 0.6	10.6 ± 1.4
$B^+ \to K^+\pi^+\pi^-$	1008 ± 44	160 ± 19	20.2 ± 0.9	18.4 ± 2.2

TABLE I. Summary of charmless yields, and yields per integrated luminosity, in 2019 Belle II data. The size of the simulated (experimental) sample corresponds to an integrated luminosity of 50 (8.7) fb^{-1}. Only the statistical contributions to the uncertainties are reported.
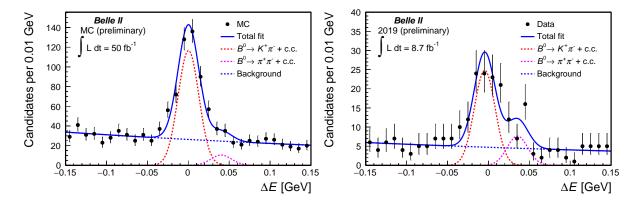
FIG. 1. Distributions of ΔE for $B^0 \to K^+\pi^-$ candidates reconstructed in (left) simulated data and (right) 2019 Belle II data selected through the baseline criteria plus an optimized continuum-suppression and kaon-enriching selection, and further restricted to $M_{\mathrm{bc}} > 5.27\,\mathrm{GeV}/c^2$. A misre-constructed $\pi^+\pi^-$ component is included with shape equal to the $K^+\pi^-$ shape and distance from the $K^+\pi^-$ peak fixed to the known value. The global position of the two peaks is determined by the fit. The projection of an unbinned maximum likelihood fit is overlaid.
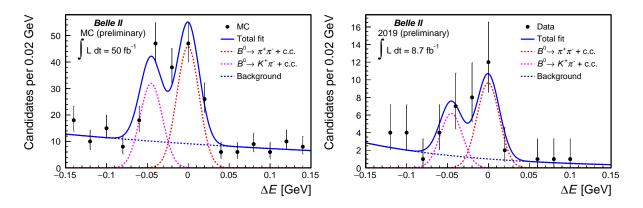

FIG. 2. Distributions of ΔE for $B^0 \to \pi^+\pi^-$ candidates reconstructed in (left) simulated data and (right) 2019 Belle II data, selected through the baseline criteria plus an optimized continuum-suppression and pion-enriching selection, and further restricted to $M_{\mathrm{bc}} > 5.27\,\mathrm{GeV}/c^2$. A misre-constructed $K^+\pi^-$ component is included with shape equal to the $\pi^+\pi^-$ shape and distance from the $\pi^+\pi^-$ peak fixed to the known value. The global position of the two peaks is determined by the fit. The projection of an unbinned maximum likelihood fit is overlaid.
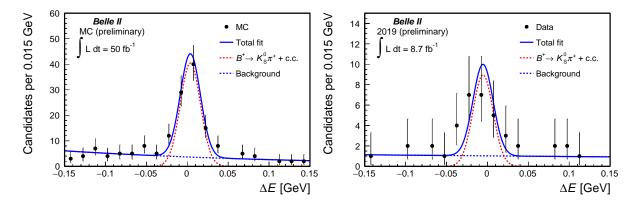
FIG. 3. Distributions of ΔE for $B^+ \to K_S^0 \pi^+$ candidates reconstructed in (left) simulated data and (right) 2019 Belle II data, selected through the baseline criteria plus an optimized continuum-suppression, and further restricted to $M_{bc} > 5.27\,\mathrm{GeV}/c^2$. The projection of an unbinned maximum likelihood fit is overlaid.
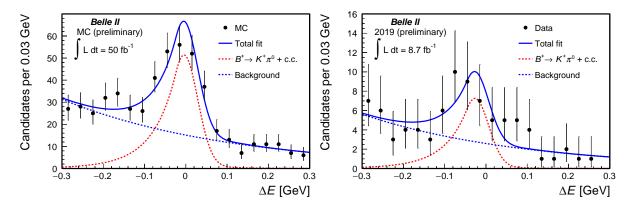

FIG. 4. Distributions of ΔE for $B^+ \to K^+ \pi^0$ candidates reconstructed in (left) simulated data and (right) 2019 Belle II data, selected through the baseline criteria plus an optimized continuum-suppression, kaon- and π^0-enriching selection, further restricted to $M_{bc} > 5.27\,\mathrm{GeV}/c^2$. The projection of an unbinned maximum likelihood fit is overlaid.
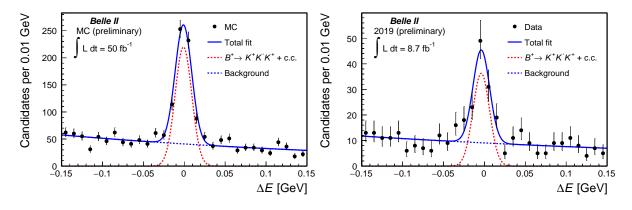

FIG. 5. Distributions of ΔE for $B^+ \to K^+ K^- K^+$ candidates reconstructed in (left) simulated data and (right) 2019 Belle II data, selected through the baseline criteria plus an optimized continuum-suppression and kaon-enriching selection, further restricted to $M_{bc} > 5.27\,\mathrm{GeV}/c^2$. The projection of an unbinned maximum likelihood fit is overlaid.
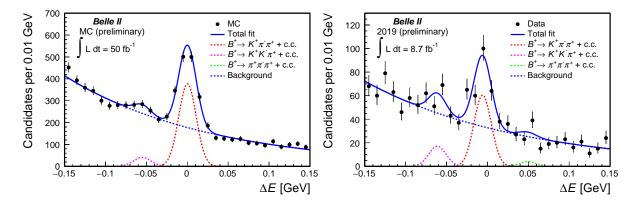
FIG. 6. Distributions of ΔE for $B^+ \to K^+\pi^-\pi^+$ candidates reconstructed in (left) simulated data and (right) 2019 Belle II data, selected through the baseline criteria plus an optimized continuum-suppression and kaon-enriching selection, further restricted to $M_{\mathrm{bc}} > 5.27\,\mathrm{GeV}/c^2$. Vetoes for peaking backgrounds are applied. Misreconstructed $K^+K^-\pi^+$ and $\pi^+\pi^-\pi^+$ components are included with shape equal to the $K^+\pi^-\pi^+$ shape and distances from the $K^+\pi^-\pi^+$ peak fixed to the known values. The global position of the three peaks is determined by the fit. The projection of an unbinned maximum likelihood fit is overlaid.

7. COMPARISON WITH BELLE

Comparison of the current two-body results with Belle's latest results on the same channels, based on the full sample corresponding to $712\,\mathrm{fb}^{-1}$ [6], provides interesting insight to assess Belle II's current and projected performance. A consistent comparison would require redoing the full analysis of Belle data to account for the differences in the statistical content of the variables and in analysis strategy. We offer a simplified comparison based on signal yields and peak purities (i.e., S/B at peak), shown in Table II. The current Belle II performance in charmless B decay reconstruction is comparable to the Belle performance.

Decay	Belle II yield/fb^{-1}	Belle II purity	Belle yield/fb^{-1}	Belle purity
$B^0 \to K^+\pi^-$	9.1 ± 1.3	≈ 10	10.6 ± 0.18	≈ 5
$B^0 \to \pi^+\pi^-$	1.8 ± 0.6	≈ 5.5	2.96 ± 0.12	≈ 2.4
$B^+ \to K^+\pi^0$	3.1 ± 0.9	≈ 3.6	5.2 ± 0.13	≈ 3.5
$B^+ \to K_{\mathrm{S}}^0\pi^+$	2.1 ± 0.6	≈ 10	4.5 ± 0.1	≈ 12

TABLE II. Comparison between Belle [6] and Belle II (this work) performance in signal yield and peak purity. Only the statistical contributions to the uncertainties are reported.

8. SUMMARY

We report on the reconstruction of various B charmless signals in 2019 Belle II data. We devise optimized event selections using simulation and apply them to the full data set collected in 2019, corresponding to $8.7\,\mathrm{fb}^{-1}$ of integrated luminosity. The ΔE distributions of the resulting samples, restricted in M_{bc}, are fit to search for charmless signals. Signal yields of approximately 80, 15, 20, 30, 90, and 160 decays are reconstructed for the channels $B^0 \to K^+\pi^-$, $B^0 \to \pi^+\pi^-$, $B^+ \to K_S^0(\to \pi^+\pi^-)\pi^+$, $B^+ \to K^+\pi^0(\to \gamma\gamma)$, $B^+ \to K^+K^-K^+$, and $B^+ \to K^+\pi^-\pi^+$, respectively, totaling nearly 400 charmless B decays (Fig. 7). Yields are generally compatible with expectations from simulation and have comparable backgrounds. This work establishes a good understanding of detector performance. In addition, it establishes solid ground to assess future projections for charmless physics measurements, such as stringent tests of the isospin sum-rule [1], for which competitive results could be available with the sample collected a year from now.
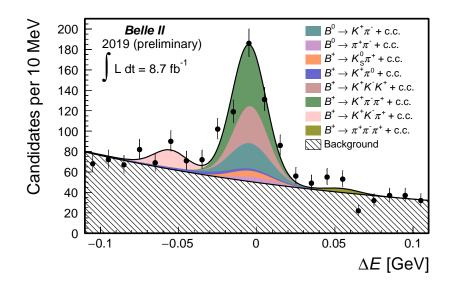
FIG. 7. Stacked ΔE distributions of charmless channels reconstructed in 2019 Belle II data with the sum of fit projections overlaid.

[1] W. Altmannshofer *et al.* (Belle II Collaboration), The Belle II Physics Book, PTEP **2019** (2019) no. 12, 123C01.

[2] B. Wach (Belle II Collaboration), First charmless B signal reconstruction in Belle II, BELLE2-NOTE-PL-2019-25.

[3] T. Abe *et al.* (Belle II Collaboration), Belle II Technical Design Report, arXiv:1011.0352.

[4] K. Akai *et al.* (SuperKEKB), SuperKEKB Collider, Nucl. Instrum. Meth. A **907** (2018) 188–199.

[5] F. Abudinén, Ph.D. Thesis, Development of a B^0 flavor tagger and performance study of a novel time-dependent CP analysis of the decay $B^0 \to \pi^0\pi^0$ at Belle II, Ludwig Maximilian University of Munich (2018), BELLE2-PTHESIS-2018-003.

[6] Y. T. Duh *et al.* (Belle Collaboration), Measurements of branching fractions and direct CP asymmetries for $B \to K\pi$, $B \to \pi\pi$ and $B \to KK$ decays, Phys. Rev. **D87** (2013) no. 3, 031103.